



# Microstructural characterization of a double pulse resistance spot welded 1200 MPa TBF steel

Manfred Stadler<sup>1</sup> · Martin Gruber<sup>2</sup> · Ronald Schnitzer<sup>1</sup> · Christina Hofer<sup>1</sup>

Received: 12 September 2019 / Accepted: 27 November 2019 / Published online: 8 December 2019  
© The Author(s) 2019

## Abstract

In the automotive industry resistance, spot welding is the dominant technology in sheet metal joining of advanced high strength steels (AHSS). In order to improve the mechanical performance of AHSS welds, in-process tempering via a second pulse is a possible approach. In this work, two different double pulse welding schemes were applied to a 1200 MPa transformation-induced plasticity (TRIP)-aided bainitic ferrite (TBF) steel. The different microstructures in the welds were characterized via light optical and scanning electron microscopy. Additionally, hardness mappings with several hundred indents were performed. It is shown that the second pulse, following a low first pulse which is high enough to produce a weld nugget that fulfills the quality criterion of a minimum spot weld diameter of  $4\sqrt{t}$ , leads to partial re-austenitization and consequently to a ferritic/martensitic microstructure after final quenching. Hardness mappings revealed that this inner FZ is harder than the surrounding FZ consisting of tempered martensite. In contrast, if the highest current without splashing is chosen for the first pulse, the same second pulse does not re-austenitize the FZ but only temper the martensite.

**Keywords** Resistance spot welding · Double pulse · AHSS · TRIP-aided bainitic ferrite · TBF

## 1 Introduction

In order to reduce the car body weight and subsequently minimize the amount of emissions, further development of advanced high strength steels (AHSS) for automotive applications is required. Steel grades from the third generation of AHSS combine high strength and ductility at lower costs than grades of the second generation [1]. Transformation-induced plasticity (TRIP)-aided bainitic ferrite (TBF) steels are promising representatives of this generation. Their superior mechanical properties are achieved by a multiphase microstructure containing bainite and a sufficient amount of retained austenite stabilized by carbon enrichment during an isothermal holding step [2–4].

Due to the combination of high operation speed and its suitability for automation, resistance spot welding (RSW) is

the dominant technology in sheet metal joining in the automotive industry [5]. The body in white of modern cars contains thousands of spot welds. Therefore, the mechanical performance and failure mode of the welds play an important role in terms of crashworthiness and consequently passenger safety. However, the relatively high content of alloying elements in AHSS compared to mild steels and the rapid cooling during RSW lead to a hard and brittle martensitic microstructure of the weld, and therefore the weldability of these steels is restricted [5–7]. Generally, AHSS resistance spot welds can be divided into the zones schematically illustrated in Fig. 1. The fusion zone (FZ) melts completely, is usually fully martensitic, and has a cast-like structure. In contrary, the heat-affected zone (HAZ) does not melt but is influenced by the heat input. It can be subdivided into the zones described in the following. The upper critical heat-affected zone (UCHAZ) consists of the UCHAZ<sub>I</sub>, also called coarse grain zone, and the UCHAZ<sub>II</sub>, also called fine grain zone. In the UCHAZ, the material is heated over the  $A_3$  temperature and therefore fully austenitized. Consequently, the microstructure is martensitic after quenching. The temperature in the intercritical heat-affected zone (ICHAZ) rises to a level between  $A_1$  and  $A_3$ , and its microstructure after quenching consists of ferrite and martensite. The peak temperature in the subcritical heat-

✉ Manfred Stadler  
manfred.stadler@unileoben.ac.at

<sup>1</sup> Department of Materials Science, Montanuniversität Leoben,  
Franz-Josef-Strasse 18, 8700 Leoben, Austria

<sup>2</sup> voestalpine Stahl GmbH, voestalpine-Strasse 3, 4020 Linz, Austria

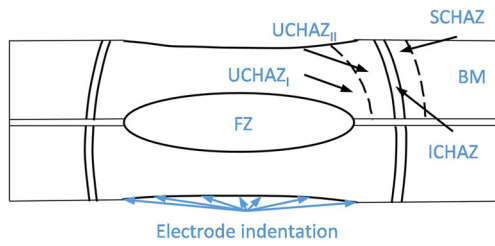


**Fig. 1** Schematic illustration of the emerging zones in a RSW from the inside out: Fusion zone (FZ), coarse grain upper critical heat-affected zone (UCHAZ<sub>I</sub>), fine grain upper critical heat-affected zone (UCHAZ<sub>II</sub>), intercritical heat-affected zone (ICHAZ), subcritical heat-affected zone (SCHA<sub>Z</sub>), and the base metal (BM)

affected zone (SCHA<sub>Z</sub>) is lower than the  $A_1$  temperature. Tempering of the microstructure occurs in this area and leads to softening [5, 8–10].

A possible approach to improve the performance of AHSS spot welds is in-process tempering via a second pulse. There are basically two different concepts of double pulsing. The first concept aims to transform the cast-like structure. In the past, several authors recommended a short cooling time between the pulses, leading to recrystallization of the outer FZ and consequently to the transformation of the cast-like structure. Eftekharimilani et al. [11] illustrated that the shape of the prior austenite grains (PAGs) changes from an elongated to an equiaxed shape at the edge of the FZ. Furthermore, it is reported that segregations at the edge of the FZ are reduced after a second pulse, and therefore the risk of intergranular failure is reduced [12]. Chabok et al. [13] stated that the second pulse lowers the residual stress at the edge of the FZ and furthermore leads to a severe softening of the SCHA<sub>Z</sub>. Moreover, the recrystallization causes an increase of high-angle grain boundaries in the UCHAZ [13]. With this concept, cracking behavior and ultimate strength during cross tension tests were improved significantly [11–17]. The other concept aims to soften the hard and therefore brittle martensitic FZ. Therefore, the cooling time is extended to a level that the temperature of the FZ reaches martensite finish ( $M_f$ ) temperature. The second pulse, usually lower than the first one, tempers the martensite

and therefore increases its ductility. In the past, this approach was successfully used to improve the mechanical performance of welds in TRIP steel [18, 19].

Although double pulse RSW of AHSS is well-documented in the literature [11–17, 20], the characterization of the occurring zones in a double pulse welded TBF steel with a tensile strength of 1200 MPa is still missing. The present work shows methods to characterize and distinguish the different zones in a temper pulse welded TBF steel and aims at understanding the ongoing tempering effects during the second pulse. Two different welding schemes were compared, and the differences regarding the microstructure are illustrated using light optical microscopy and scanning electron microscopy. Moreover, hardness mappings with several hundred indents per weldment were performed to investigate the influence of the second pulse on the hardness and to correlate it to the observed microstructure.

## 1.1 Experimental

A 1200 MPa TBF steel with a nominal composition of 0.2C/1.5Si/2.5Mn (wt%) was investigated. The steel sheets with a thickness of 1.34 mm were electrolytically galvanized, having a coating thickness of 6.6–8.6  $\mu\text{m}$  per side as specified in VDA 239–100 [21]. RSW was performed using a Nimak MFDC-1000 Hz pedestal-type welding machine, equipped with a AutoSpatz regulator, delivering constant current and F1–16–20–6 electrodes with a force of 4.5 kN as recommended in VDEh SEP1220–2 [22]. In this paper, two different double pulse welding sequences were applied which are illustrated in Fig. 2. For the sequence illustrated in Fig. 2 (a), the first pulse is just high enough to produce a weld nugget that fulfills the quality criterion of a minimum spot weld diameter of  $4\sqrt{t}$ , where  $t$  is the sheet thickness. Although this criterion is not completely reliable for AHSS welds, it was chosen in the present study as it is well-known as a quality criterion for spot welds. The sample welded with this minimum current ( $I_{\min}$ ) is hereinafter referred to as sample  $I_{\min}$ . For the first

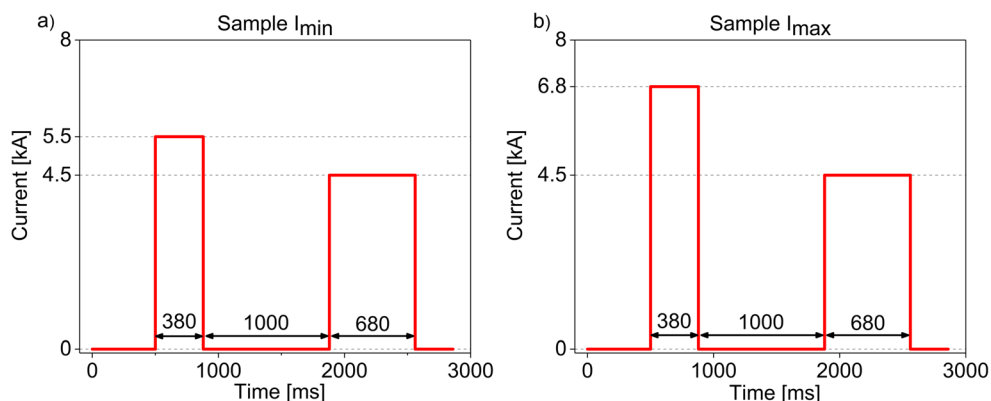


**Fig. 2** Welding sequences for (a) sample  $I_{\min}$  and (b) sample  $I_{\max}$

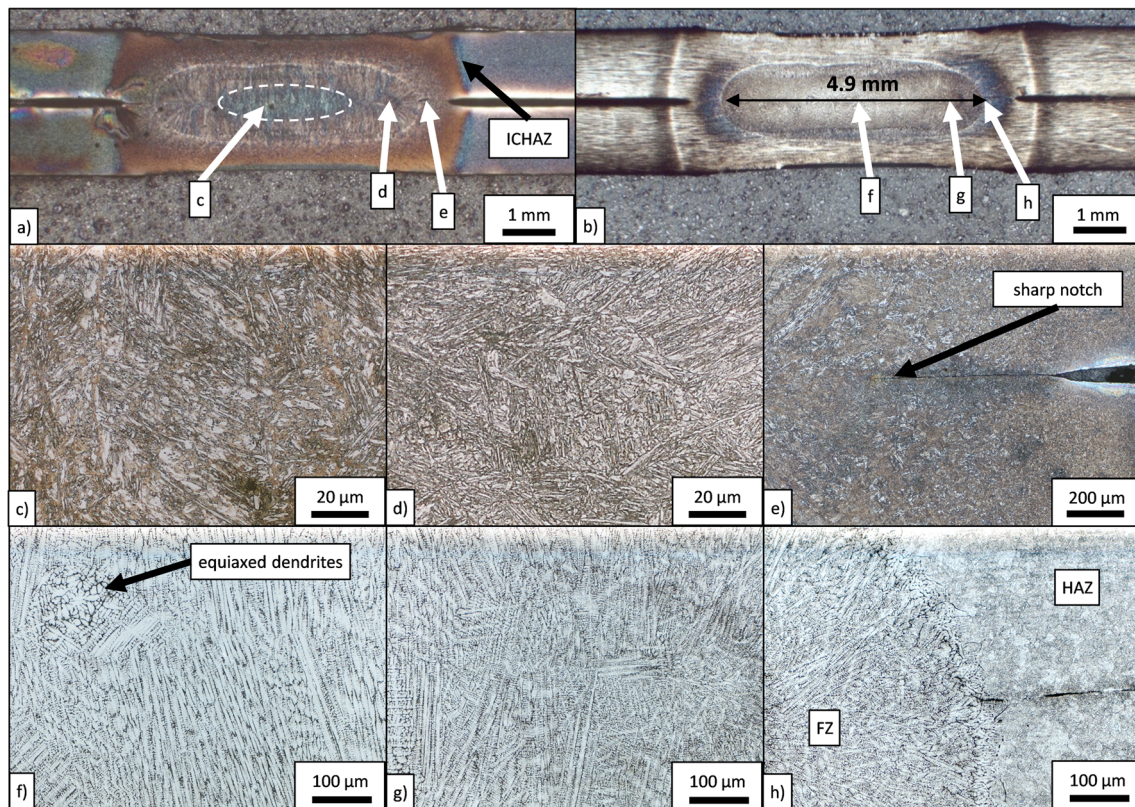


**Fig. 3** Overview of sample  $I_{\min}$  after etching with (a) Nital and (b) picric acid. Detailed images of (c) the inner FZ, (d) the outer FZ, and (e) the transition between FZ and HAZ after Nital etching. Detailed images of (f)

the inner FZ, (g) the outer FZ, and (h) the transition from FZ to HAZ after etching with picric acid

pulse of the sequence illustrated in Fig. 2 (b), the highest current without splashing ( $I_{\max}$ ) was chosen as described in VDEh SEP1220–2 [22]. The sample welded with this sequence is hereinafter referred to as sample  $I_{\max}$ . In the preliminary investigation, a temper pulse of about two-thirds of  $I_{\max}$ , approximately 4.5 kA, turned out to be ideal for samples welded at the splashing limit. This current of 4.5 kA was chosen for the second pulse of both sequences. For each sequence, a squeeze time of 500 ms was followed by a 380 ms welding time, a cooling time of 1000 ms, a 680 ms lasting second pulse, and a hold time of 300 ms. The extraordinary long cooling time of 1000 ms was chosen to be sure that the temperature prior to the second pulse is safely below  $A_1$  and to

clearly differentiate the present concept from the recrystallization pulse concept.

For microstructural characterization, cross sections were ground, polished, and finally etched with 3% Nital solution for a few seconds for light optical microscopy (LOM) investigations and for less than 1 s for investigations via scanning electron microscopy (SEM). To visualize the dendrites and the prior austenite grains, a mixture of cold saturated picric acid, Natriumdodecylbenzolsulfonat, and hydrochloric acid was used. LOM images were taken with a Zeiss M1M Imager equipped with a AxioCam MRc5 camera, both from Zeiss. SEM investigations were performed on Zeiss EVO 50 using secondary electron contrast.

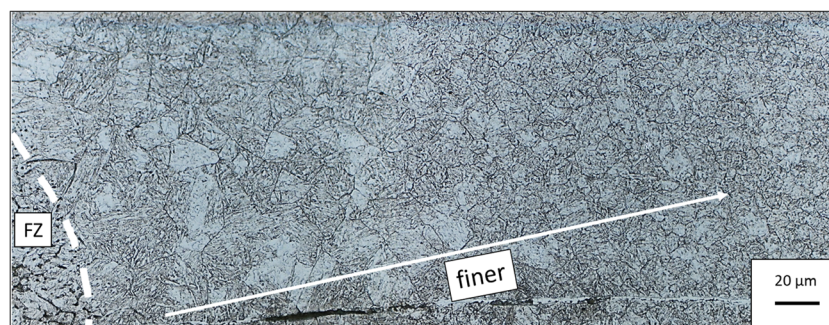


**Fig. 4** LOM image of the UCHAZ of sample  $I_{\min}$  after etching with picric acid. PAGs are visible, and their size decreases with increasing distance to the FZ

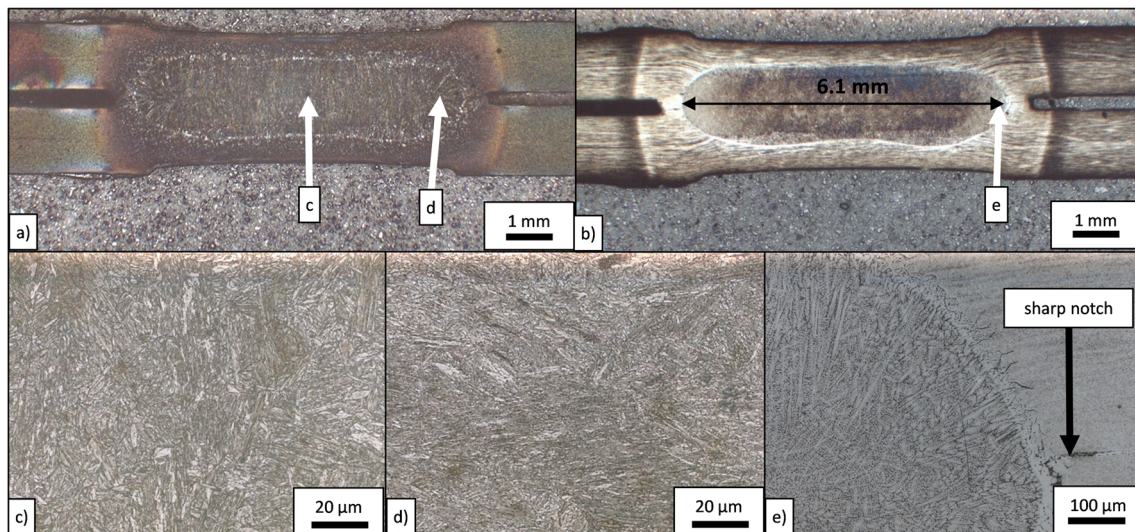


**Fig. 5** Overview of sample  $I_{\max}$  after etching with (a) Nital and (b) picric acid. Detailed images of (c) the center of the FZ, (d) the edge of the FZ after Nital etching, and (e) the transition from FZ to HAZ after etching with picric acid

For Vickers hardness mappings, a Qness Q60A+ hardness tester was used. The distance between the indents was 150  $\mu\text{m}$ , and the load was 300 g.

## 2 Results

### 2.1 Microstructural characterization via LOM

In order to characterize the microstructure of sample  $I_{\min}$ , LOM images were taken. Figure 3 (a) shows an overall image of the weld after Nital etching and Fig. 3 (b) after etching with picric acid. Nital attacks the FZ nonuniformly and separates it into an inner and an outer part. Furthermore, this etching method offers an easy way to distinguish the martensitic UCHAZ from the ICHAZ (marked by an arrow in Fig. 3 (a)), since the ferritic areas are stronger attacked due to their lower carbon content [23]. Comparing Fig. 3 (c) and Fig. 3 (d), it can be seen that the microstructure of the inner FZ indeed differs from the outer one. The inner zone seems coarser and more heterogeneous, while the outer zone is homogeneous. Figure 3 (e) illustrates that Nital is not the most suitable etching method for distinguishing the FZ from the HAZ as they are both martensitic. The notch between the sheets is sharp, as indicated by an arrow in Fig. 3 (e)), which is typical for RSW [5]. It is reported that picric acid attacks elements like phosphorus [24]. Since phosphorus tends to segregate between the dendrites [25], it is an appropriate method to visualize solidification structure of the FZ. The size of the FZ is approximately 4.9 mm. Figure 3 (f) and Fig. 3 (g) show the orientation of the dendrites alongside the heat dissipation. In the case of the inner zone (Fig. 3 (f)), the water-cooled electrodes represent the dominant heat sinks. As the inner FZ solidifies last, therefore the temperature gradient is relatively small compared to the outer FZ; also

equiaxed dendrites appear. At the edge of the FZ, depicted in Fig. 3 (h), the orientation of the dendrites changes, since the heat mainly dissipates toward the BM. This etching clearly visualizes the transition from the FZ to the HAZ, since phosphorus in the FZ is mainly segregated between the dendrites, while it preferentially segregates at the grain boundaries in the UCHAZ.

The main metallographic application of picric acid is the visualization of the PAGs in a martensitic microstructure [26]. Figure 4 shows the PAGs in the UCHAZ of sample  $I_{\min}$ . The PAG size of the area in close proximity to the FZ is about 20  $\mu\text{m}$  and larger. With a greater distance to the FZ, the PAG size decreases, and therefore the UCHAZ<sub>I</sub> merges into the UCHAZ<sub>II</sub>. This transition takes place within approximately 100–200  $\mu\text{m}$ .

LOM images of sample  $I_{\max}$  were taken as well. Figure 5 (a) shows an overall image of the weld after Nital etching and Fig. 5 (b) after etching with picric acid. Compared to sample

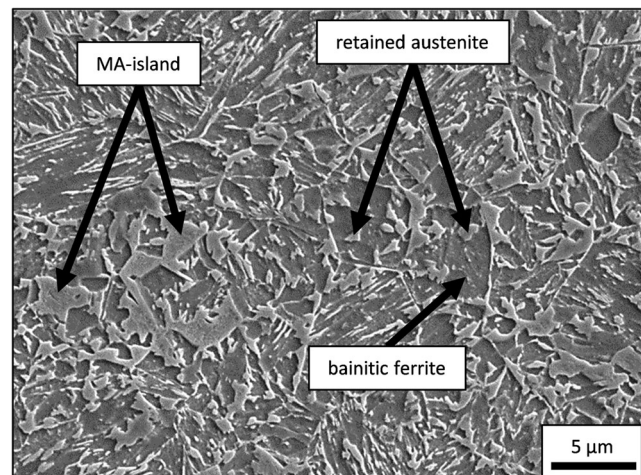


**Fig. 6** SEM image of the BM of the investigated TBF steel

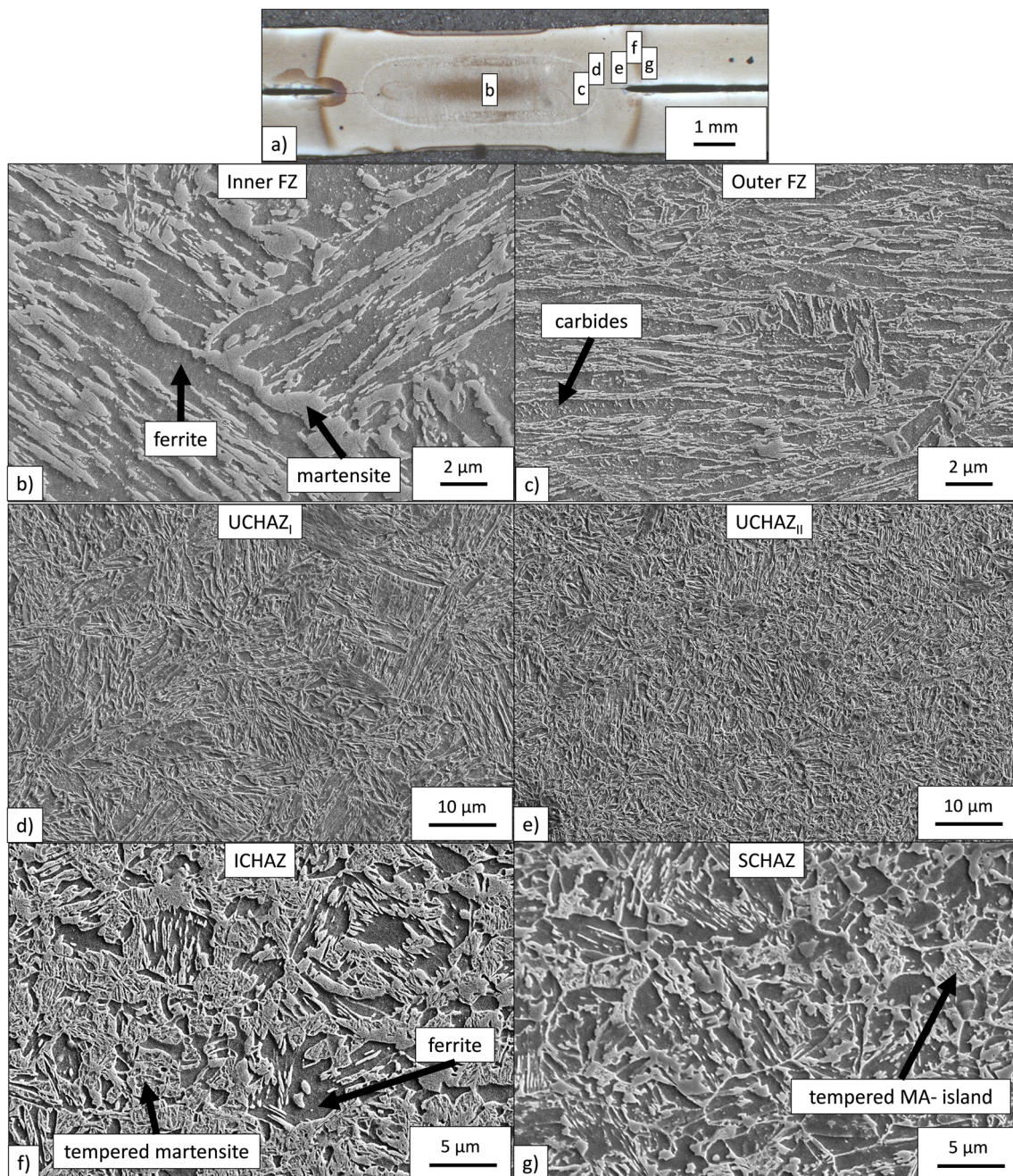


**Fig. 7** (a) Overview LOM image of sample  $I_{\min}$  after Nital etching. SEM image of (b) the inner FZ showing a ferritic/martensitic microstructure, (c) the outer FZ consisting of tempered martensite with small carbides, (d)

the UCHAZ<sub>I</sub> containing coarse grained martensite, and (e) the UCHAZ<sub>II</sub> containing fine grained martensite. The martensite in (f) the ICHAZ and the MA islands in (g) the SCHAZ show a tempered structure

$I_{\min}$ , the gap between the sheets is larger, but the resulting notch is still sharp, as indicated by an arrow in Fig. 5 (e). The larger heat input during the first pulse also results in a larger FZ (6.1 mm) and a deeper indentation depth. Figure 5 (c) and Fig. 5 (d) indicate that the microstructure in the center and at the edge of the FZ is martensitic and, in contrast to sample  $I_{\min}$ , not divided into two different parts. The edge of the FZ after etching with picric acid is depicted in Fig. 5 (e).

While the interface between FZ and HAZ can be well-recognized, the PAG boundaries were not revealed in this sample.

## 2.2 Microstructural characterization via SEM

For higher-resolution imaging of the microstructure, SEM was performed. From the SEM image of the BM in Fig. 6, it is apparent that the BM of a TBF steel consists of a multiphase

microstructure. Due to the low carbon content, the bainitic ferrite is strongly attacked by the etchant Nital and therefore appears deeper. The small, round islands within the bainitic matrix are retained austenite. The larger, angular regions show a slight substructure at higher magnification and are a combination of austenite and martensite, the so-called MA-islands [27].

The occurring zones of sample  $I_{\min}$  are characterized in the following. Figure 7 (a) gives an overview and indicates where the images were taken. The microstructure of the inner FZ, which is illustrated in Fig. 7 (b), consists of ferrite and untempered martensite and is much coarser compared to the outer FZ shown in Fig. 7 (c). The martensite in the outer FZ exhibits small, regularly oriented carbides which indicate pronounced tempering. These carbides are missing in the inner FZ. The UCHAZ<sub>I</sub> and UCHAZ<sub>II</sub> depicted in Fig. 7 (d) and Fig. 7 (e) mainly differ regarding the much coarser martensitic microstructure in the UCHAZ<sub>I</sub>. Tempering effects in the form of small carbides are less pronounced. As can be seen in Fig. 7 (f), the ICHAZ consists of a ferritic and martensitic microstructure. However, the martensitic areas show a pronounced inner structure characteristic of tempered martensite. The microstructure of the SCHAZ, which is shown in Fig. 7 (g), is similar to the BM, consisting of bainitic ferrite, MA islands, and retained austenite. However, some of the MA islands show a distinct inner structure compared to the flat MA islands of the BM. This inner structure is attributed to temper effects typical for the SCHAZ of a martensite containing AHSS [28].

SEM micrographs of sample  $I_{\max}$  were taken as well. The microstructure of the center of the FZ of this sample, which is shown in Fig. 8, consists of tempered martensite and is comparable to the outer FZ of sample  $I_{\min}$  (Fig. 7 (c)) rather than to the inner FZ (Fig. 7 (b)). The edge of the FZ, UCHAZ, and SCHAZ of sample  $I_{\max}$  was also investigated but did not differ significantly from the zones in sample  $I_{\min}$  and are therefore not depicted.

The martensitic areas in the ICHAZ of sample  $I_{\max}$  depicted in Fig. 9 do not show pronounced signs of tempering.

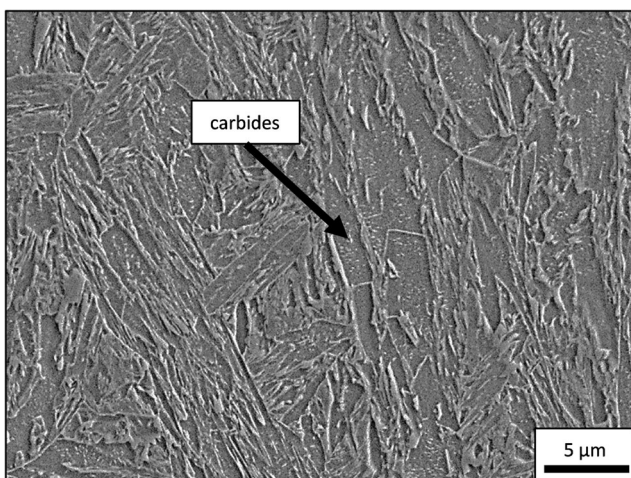


**Fig. 8** SEM image of the center of the FZ of sample  $I_{\max}$  showing tempered martensite

Only a small amount of them have an inner substructure, while the majority is smooth.

### 2.3 Hardness mapping

In order to investigate the influence of tempering on the hardness profile of the weldment, hardness mappings were recorded. As illustrated in Fig. 10 (a), the different microstructures of the inner and the outer FZ are also reflected in the hardness mappings of sample  $I_{\min}$ . The hardness of the inner FZ is about 420 HV and therefore 50 to 60 HV harder than the outer FZ. The hardness level of the UCHAZ rises from 420 to 480 HV with increasing distance to the FZ and drops to 420 HV in the ICHAZ. With a hardness of approximately 350 HV, the SCHAZ is about 70 HV softer than the BM. The hardness mapping of sample  $I_{\max}$  is depicted in Fig. 10 (b). In contrast to sample  $I_{\min}$ , the hardness of the FZ of sample  $I_{\max}$  increases from the inside out, from about 360 to 420 HV. The hardest area is the UCHAZ with more than 500 HV, and therefore it is much harder than the UCHAZ of sample  $I_{\min}$ .

## 3 Discussion

An inner FZ is formed in sample  $I_{\min}$ , as can be seen in Fig. 3. This sample was welded with a lower current at the first pulse. The metallographic constituents of this inner fusion zone were identified via SEM. Figure 7 (b) illustrates that its microstructure consists of two phases, which are attacked differently by Nital. According to Angeli et al. [23], the chemical potential of the individual phases in low alloyed steels depends mainly on their carbon content. Thus it can be inferred that the stronger attacked areas correspond to ferrite, while the less attacked phase is associated with carbon rich martensite. Since the martensitic areas of this dual-phase microstructure show no signs of tempering, they are most likely transformed during the final quenching. Hence, the temperature of the inner FZ must have been between  $A_1$  and  $A_3$  prior to the final quenching, causing partial re-austenitization during the second pulse. In contrast, the microstructure of the outer FZ, depicted in Fig. 7 (c), consists of tempered martensite as proofed by the occurring carbides. Consequently, the peak temperature of this area must have been lower than  $A_1$  during the second pulse since only one phase is present. Hernandez et al. [20] also observed a strong correlation between the magnitude of the pulse and the evolving microstructure by varying the second pulse instead of the first pulse as in this work. They simulated the temperature of the FZ during the second pulse and stated that a current of 5 kA results in a temperature below  $A_1$ , leading to softening, while the temperature after a second pulse of 7 kA was above  $A_3$  resulting in re-austenitization. The hardness mapping of sample  $I_{\min}$ , depicted in Fig. 10 (a), shows that the dual-phase microstructure of the inner FZ is 50 to 60 HV harder than the

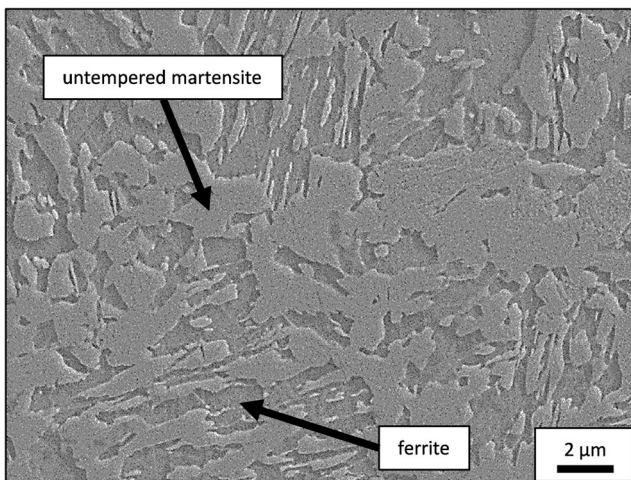


**Fig. 9** SEM image of the ICHAZ of sample  $I_{\max}$  consisting of ferrite and untempered martensite

tempered martensite of the outer one. On the contrary, as can be seen in Fig. 5 and Fig. 8, the entire FZ of sample  $I_{\max}$  consists of tempered martensite. This indicates that the peak temperature during the second pulse must have been lower than the  $A_1$  temperature since no phase transformation occurred. The hardness of the weldment rises from the inside out with a hardness peak in the  $UCHAZ_{II}$  as illustrated in Fig. 10 (b). This is due to the decreasing peak temperature during the second pulse and consequently the less pronounced tempering effects with increasing distance to the center of the FZ. With a hardness of more than 500 HV,  $UCHAZ_{II}$  of sample  $I_{\max}$  is much harder than its sample  $I_{\min}$  counterpart. This can be explained by the higher heat input during the first pulse in sample  $I_{\max}$  resulting in a bigger weld nugget as can be seen comparing Fig. 3 (b) and Fig. 5 (b). Due to the larger distance between the center of the FZ and the  $UCHAZ_{II}$  in sample  $I_{\max}$ , the temperature does not rise to a level where effective tempering occurs during the second pulse. The comparison of the ICHAZ of both samples depicted in Fig. 7 (f)

and Fig. 9, also illustrates this circumstance. The martensitic areas in the ICHAZ of sample  $I_{\min}$  (Fig. 7 (f)) show a clear inner substructure due to tempering while these areas are smooth in the ICHAZ of sample  $I_{\max}$ . This indicates that the temperature during the second pulse of sample  $I_{\max}$  is lower in this area.

Generally, for RSW, the heat dissipates toward the cooled electrodes and the BM. For thin sheets, the cooling mechanism of small welding nuggets is dominated by heat loss toward the cooled electrodes [29]. This can be visualized by the dendrites in the FZ, since they show a preferred orientation along the maximal thermal gradient [11]. In the inner FZ (Fig. 3 (f)), the dendrites are mainly oriented in vertical direction, illustrating that the heat dissipates to the cooled electrodes, while the dendrites at the edge of the FZ are mainly oriented in horizontal direction, toward the BM (Fig. 3 (h) and Fig. 5 (e)). Comparing Fig. 3(b) and Fig. 5 (b), it can be seen that due to the lower heat input in sample  $I_{\min}$ , the electrode indentation depth of this sample is much lower compared to sample  $I_{\max}$ . Consequently, the distance between the cooled electrodes and the liquid weld pool is larger, which results in a lower cooling rate according to Pouranvari and Marashi [5]. This may lead to a higher temperature in sample  $I_{\min}$  after the cooling time compared to sample  $I_{\max}$  and consequently to a higher temperature during the second pulse in this sample. Moreover, for the heat generation and temperature evolution in the nugget, the current plays an important role [30]. Compared to sample  $I_{\max}$ , due to the lower current during the first pulse, the nugget diameter of sample  $I_{\min}$  is smaller after the first pulse. This means that during the second pulse, the ratio of the passing current to the size of the FZ is larger for sample  $I_{\min}$ , and consequently, more heat is generated. This circumstance may also be responsible for the re-austenitization of the inner FZ of sample  $I_{\min}$  during the second pulse. However, the prediction of the exact temperature distribution and nugget size evolution due to a given current is highly

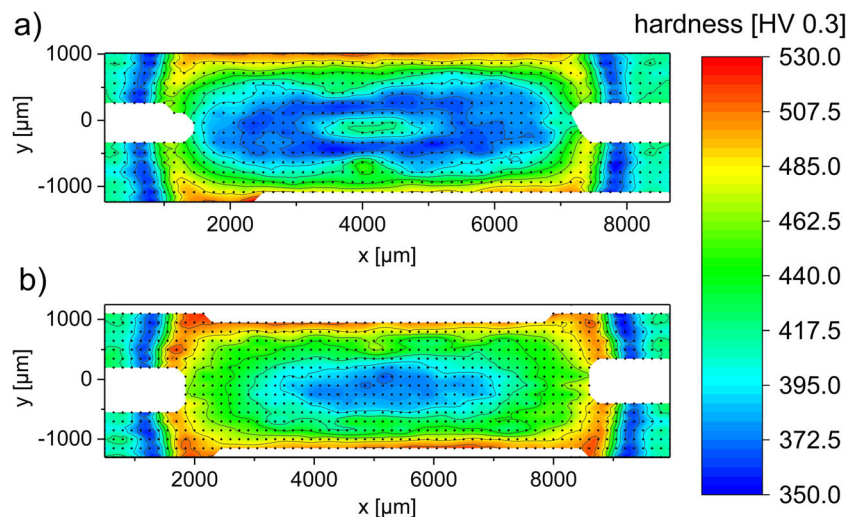


**Fig. 10** Vickers hardness mapping of (a) sample  $I_{\min}$  and (b) sample  $I_{\max}$

complex and depends on many aspects [31] and is beyond the scope of this paper.

Besides the visualization of dendrites, picric acid is widely used to illustrate the PAGs in martensitic steels [26], and therefore it is an appropriate etching method to characterize the UCHAZ of spot welds. For sample  $I_{\min}$ , this etching achieved valuable results, as can be seen in Fig. 4, where a significant difference in PAG size as a function of the distance to the FZ can be seen. However, it is noteworthy that the PAG boundaries are not visible in sample  $I_{\max}$ . Generally, tempering is an effective way to improve the etching result for AHSS [32]. During this heat treatment, elements like phosphorus segregate to the PAG boundaries, resulting in an attack during the subsequent etching. Since the PAG boundaries of sample  $I_{\max}$  are not revealed, it can be concluded that the degree of tempering of the UCHAZ is lower compared to sample  $I_{\min}$ . Consequently, picric acid-based etching is not only a good way to characterize the UCHAZ but also to estimate the degree of tempering in double pulse RSW.

## 4 Conclusion

In the present work, RSW of a 1200 MPa TBF steel was performed using two different double pulse welding schemes. The different zones were characterized by LOM, SEM, and hardness mappings, and the following conclusions can be drawn:

- 1) If the first pulse is low and the weld nugget therefore small, an inner FZ with a different microstructure than the residual FZ forms after the second pulse. This inner FZ shows no signs of tempering and consists of ferrite and untempered martensite as a result of a partial re-austenitization during the second pulse. The hardness map reveals that this inner FZ is harder than the outer FZ consisting of tempered martensite.
- 2) If the first pulse is high and the weld nugget is therefore large, the entire FZ is tempered during the second pulse. The hardness map reveals that due to the temperature gradient, the tempering effect decreases from the inside out. Observation of the microstructure in the SEM illustrated that the ICHAZ is not tempered significantly by the second pulse, since the distance from the FZ is large.
- 3) A higher energy input during the first pulse is associated with a deeper electrode indentation depth compared to a lower first pulse. This results in a faster cooling rate of the center of the FZ due to the shorter distance to the liquid melt pool. Furthermore, due to the larger weld nugget of sample  $I_{\max}$ , the ratio of current to the size of the FZ during the second pulse is lower, and less heat is generated. This contributes to the inhibited re-austenitization and the microstructure of the inner FZ of sample  $I_{\max}$  consequently consists of tempered martensite.
- 4) Etching with picric acid visualizes the PAGs in the strongly tempered UCHAZ of sample  $I_{\min}$  but does not attack the PAG boundaries of sample  $I_{\max}$ . This is because due to severe tempering, elements like phosphorus segregate to the grain boundaries extensively. Thus, this etching method is capable of estimating the degree of tempering of the UCHAZ comparatively between two double pulse welded samples.

**Acknowledgements** Open access funding provided by Montanuniversität Leoben.

**Funding information** Funding of the Austrian BMVIT (846933) in the framework of the program “Production of the future” and the “BMVIT Professorship for Industry” is gratefully acknowledged.

**Open Access** This article is licensed under a Creative Commons Attribution 4.0 International License, which permits use, sharing, adaptation, distribution and reproduction in any medium or format, as long as you give appropriate credit to the original author(s) and the source, provide a link to the Creative Commons licence, and indicate if changes were made. The images or other third party material in this article are included in the article’s Creative Commons licence, unless indicated otherwise in a credit line to the material. If material is not included in the article’s Creative Commons licence and your intended use is not permitted by statutory regulation or exceeds the permitted use, you will need to obtain permission directly from the copyright holder. To view a copy of this licence, visit <http://creativecommons.org/licenses/by/4.0/>.

## References

1. Matlock DK, Speer JG (2009) Third generation of AHSS: microstructure design concepts. In: Haldar A, Suwas S, Bhattacharjee D (eds) Microstructure and texture in steels. Springer London, London, pp 185–205
2. Hofer C, Leitner H, Winkelhofer F et al (2015) Structural characterization of “carbide-free” bainite in a Fe–0.2C–1.5Si–2.5Mn steel. Mater Charact 102:85–91
3. Hofer C, Winkelhofer F, Clemens H et al (2016) Morphology change of retained austenite during austempering of carbide-free bainitic steel. Mater Sci Eng A 664:236–246
4. Hofer C, Primig S, Clemens H et al (2017) Influence of heat treatment on microstructure stability and mechanical properties of a carbide-free bainitic steel. Adv Eng Mater 19(4):1600658
5. Pouranvari M, Marashi SPH (2013) Critical review of automotive steels spot welding: process, structure and properties. Sci Technol Weld Join 18(5):361–403
6. Den Uijl NJ, Smith S (eds) (2006) Resistance spot welding of advanced high strength steels for the automotive industry. In: 4th International Seminar on Advances in Resistance Welding, Wels, Austria (pp. 30–60)
7. Pouranvari M, Marashi SPH (2013) Key factors influencing mechanical performance of dual phase steel resistance spot welds. Sci Technol Weld Join 15(2):149–155
8. Pouranvari M, Sobhani S, Goodarzi F (2018) Resistance spot welding of MS1200 martensitic advanced high strength steel: microstructure-properties relationship. J Manuf Process 31:867–874



9. Pouranvari M, Asgari HR, Mosavizadch SM et al (2013) Effect of weld nugget size on overload failure mode of resistance spot welds. *Sci Technol Weld Join* 12(3):217–225
10. Lu Y, Peer A, Abke T et al (2018) Subcritical heat affected zone softening in hot-stamped boron steel during resistance spot welding. *Mater Des* 155:170–184
11. Eftekharimilani P, van der Aa EM, Hermans MJM et al (2017) Microstructural characterisation of double pulse resistance spot welded advanced high strength steel. *Sci Technol Weld Join* 22(7):545–554
12. Eftekharimilani P, van der Aa EM, Hermans MJM et al (2017) The microstructural evolution and elemental distribution of a 3rd generation 1 GPa advanced high strength steel during double pulse resistance spot welding. *Welding World* 61(4):691–701
13. Chabok A, van der Aa EM, De Hosson JTM et al (2017) Mechanical behavior and failure mechanism of resistance spot welded DP1000 dual phase steel. *Mater Des* 124:171–182
14. Matsuchita M, Taniguchi K, Oi K (2013) Development of next generation resistance spot welding technologies contributing to auto body weight reduction. *JFE Technical Report* 18:111–117
15. Van der Aa EM, Amirthalingam M, Winter J, Hanlon DN, Hermans MJM, Rijnders M, Richardson IM (ed) (2015) improved resistance spot weldability of 3rd generation AHSS for automotive applications. In: 11th international seminar on numerical analysis of Weldability, Graz, Austria
16. Sawanishi C, Ogura T, Taniguchi K et al (2013) Mechanical properties and microstructures of resistance spot welded DP980 steel joints using pulsed current pattern. *Sci Technol Weld Join* 19(1): 52–59
17. Liu XD, Xu YB, Misra RDK et al (2019) Mechanical properties in double pulse resistance spot welding of Q&P 980 steel. *J Mater Process Technol* 263:186–197
18. Chuko WL, Gould JE (2002) Development of appropriate resistance spot welding practice for transformation-hardened steels. *Weld J* 81(1):1–8
19. Shi G, Westgate SA (2005) Techniques for improving the weldability of TRIP steel using resistance spot welding. In: paper for 1st international conference of the high strength steel, (pp. 1-13)
20. Hernandez VB, Okita Y, Zhou Y (2012) Second pulse current in resistance spot welded TRIP steel: Effects on the microstructure and mechanical behavior. *Impulse*:91
21. Verband Der Automobilindustrie E. V. (2016) VDA 239–100: Flacherzeugnisse aus Stahl zur Kaltumformung
22. Stahl-Eisen-Prüfblätter (SEP) des Stahlinstituts VDEh SEP 1220–2: Testing and documentation guideline for the joinability of thin sheet of steel-Part 2: Resistance Spot Welding
23. Angeli J, Fureder E, Panholzer M et al (2006) Etching techniques for characterizing the phases of low-alloy dual-phase and TRIP steels. *Practical Metallography* 43(10):489–504
24. Christien F, Le Gall R, Saindrenan G (2003) Phosphorus grain boundary segregation in steel 17-4PH. *Scr Mater* 48:11–16
25. Amirthalingam M, van der Aa EM, Kwakemaak C et al (2015) Elemental segregation during resistance spot welding of boron containing advanced high strength steels. *Weld World* 59(5):743–755
26. Bechet S, Beaujard L (1955) New reagent for the micrographical demonstration of the austenite grain of hardened or hardened-tempered steels. *Revue de Métallurgie* 52:830–836
27. Hofer C, Bliznuk V, Verdiere A et al (2018) High-resolution characterization of the martensite-austenite constituent in a carbide-free bainitic steel. *Mater Charact* 144:182–190
28. Hernandez VH, Panda SK, Kuntz ML et al (2010) Nanoindentation and microstructure analysis of resistance spot welded dual phase steel. *Mater Lett* 64(2):207–210
29. Kim EW, Eagar TW (1988) Parametric analysis of resistance spot welding lobe curve. *SAE Trans*:107–118
30. Deutscher Verband Für Schweißen Und Verwandte Verfahren E.V. DVS 2902–4: Widerstandspunktschweißen von Stählen bis 3 mm Einzeldicke - Grundlagen, Vorbereitung und Durchführung
31. Williams NT, Parker JD (2004) Review of resistance spot welding of steel sheets part 1 Modelling and control of weld nugget formation. *Int Mater Rev* 49(2):45–75
32. Esterl R, Sonnleitner M, Stadler M et al (2018) Microstructural characterization of ultra-high strength martensitic steels. *Practical Metallography* 55(4):203–222

**Publisher's note** Springer Nature remains neutral with regard to jurisdictional claims in published maps and institutional affiliations.